

High-Efficiency Synergistic Effect of Supramolecular Nanoparticles Based on Cyclodextrin Prodrug on Cancer Therapy

Xianyin Dai, Bing Zhang, Weilei Zhou, and Yu Liu*



Cite This: *Biomacromolecules* 2020, 21, 4998–5007



Read Online

ACCESS |



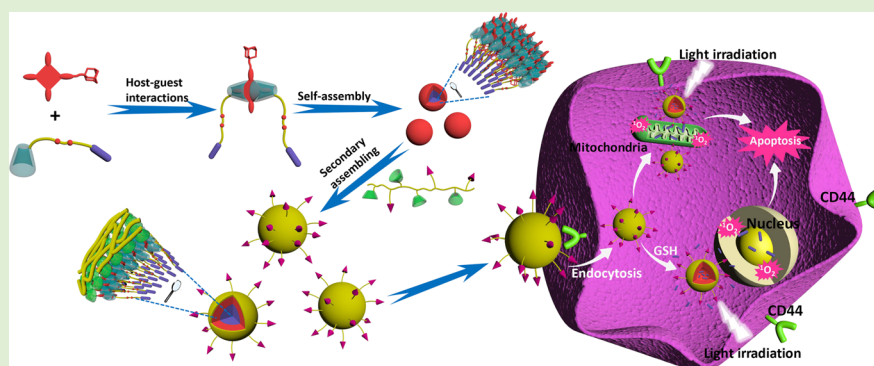
Metrics & More



Article Recommendations



Supporting Information



ABSTRACT: Novel cyclodextrin-prodrug supramolecular nanoparticles (NPs) with cooperative-enhancing cancer therapy were constructed from a reduction-sensitive disulfide bond-linked permethyl- β -cyclodextrin-camptothecin prodrug, water-soluble adamantane-porphyrin photosensitizer, and hyaluronic acid grafted by triphenylphosphine and β -cyclodextrin through an orthogonal host–guest recognition strategy, displaying uniform nanoparticles with a diameter around 100 nm as revealed by dynamic light scattering, transmission electron microscopy, scanning electron microscopy, and atomic force microscopy. Compared with 293T normal cells, the supramolecular NPs could be easily taken up by mitochondria of A549 cancer cells, then release the active anticancer drug camptothecin (CPT) in situ via the cleavage of the disulfide bond by the overexpressed glutathione, and could initiate the effective singlet oxygen ($^1\text{O}_2$) generation by porphyrin under light irradiation, ultimately resulting in severe mitochondrial dysfunction and a rising cell death rate with increasing micromolar concentration of NPs. These multicomponent supramolecular nanoassemblies effectively combined the two-step synergistic chemo-photodynamic therapy of reduction–release of CPT and light-triggered $^1\text{O}_2$ generation within cancer cells presenting the synergistic effect of supramolecular nanoparticles on cancer therapy, which provide a new approach for efficient step-by-step cancer therapy.

INTRODUCTION

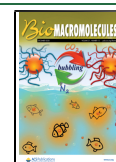
Supramolecular nanotherapeutics has gradually evolved as a promising approach for current cancer treatment.^{1–5} More and more macrocyclic prodrugs including cyclodextrins,^{6,7} calixarenes,^{8,9} pillararenes,^{10,11} and cucurbiturils^{12,13} have been successfully designed and applied into anticancer treatment, which opened up new approaches for cancer therapy. It has been proven that both the water solubility and biocompatibility of the drug could be largely improved through specific chemical modification or encapsulation by macrocyclic compounds.¹⁴ Meanwhile, only in the tumor microenvironment could the prodrugs release the corresponding active anticancer drug, which greatly reduces its adverse effects toward normal tissues.¹⁵ For example, Isaacs et al. developed a metal–organic polyhedron assisting with cucurbit[8]uril as a prodrug delivery vehicle, thus achieving the enhanced cellular uptake and cytotoxicity derived from cleavage of the acid-sensitive acylhydrazone linkage.¹⁶ Schmuck et al. reported controllable supramolecular prodrug nanocarriers with differ-

ent morphologies based on host–guest recognition between pillar[5]arene-based prodrug WP5-DOX and Arg-Gly-Asp (RGD)-modified sulfonate guest for targeted drug delivery accompanied with enhanced antitumor efficacy and reduced side effects.¹⁷ Among these various macrocyclic compounds used for fabricating kinds of supramolecular prodrug systems, cyclodextrins (CDs) as a class of cyclic oligosaccharides have received growing attention and been extensively employed in the biological field due to their low cost, convenience of modification, negligible toxicity, good biocompatibility, and unique host–guest properties.^{18,19} More recently, Chen et al.

Received: August 10, 2020

Revised: September 11, 2020

Published: September 18, 2020



fabricated a supramolecular theranostic nanomedicines through the polymerization of CPT-modified β -CDs consisting of cleavable disulfide bonds, which exerted enhanced drug stability and anticancer activity with rather low systemic toxicity and long-term immunotoxicity.²⁰ These findings apparently present the great potential of supramolecular prodrugs in cancer treatment.

Combination therapy of prodrugs and other therapies has thrived as an efficient strategy to increase therapeutic efficiency. Among them, photodynamic therapy (PDT), benefiting from its inherent advantages such as noninvasive characteristics, fewer side effects, and free of drug resistance, has been thoroughly studied in clinic to treat many cancers.^{21–23} Under the irradiation of light with a specific wavelength, the photosensitizer absorbs energy and reacts with nearby oxygen to generate reactive oxygen species (ROS), which in turn directly causes cell damage and even results in cell death.²⁴ Out of various photosensitizers, porphyrin and its derivatives are widely studied and used in photodynamic therapy because of their excellent photosensitive properties.²⁵ However, their $^1\text{O}_2$ generation ability may be seriously suppressed due to the aggregation-induced quenching (AIQ) effect, which greatly limits the PDT efficiency.^{26–28} Therefore, diminishing the aggregation between porphyrin units will be a valid solution to improve the PDT therapeutic effect.²⁹

Although both prodrug assembly and photodynamic therapy perform a vital role in cancer treatment, the combinational therapy based on a supramolecular assembly strategy that could integrate macrocyclic prodrugs and PDT is rarely reported, which is a new trend and provides new methods for synergistic cancer treatment.^{30–33} For instance, Zhao et al. recently developed a supramolecular system with an optimized loading ratio of the photosensitizer and prodrug for NIR-activated combination therapy and achieved excellent therapeutic effect.³⁴ Herein, we fabricated cyclodextrin-prodrug nanoparticles (NPs) capable of cancer-mitochondria dual targeting and step-by-step chemo-photodynamic therapy in situ. This rationally designed hierarchical nanoassemblies, composed of triphenylphosphine (TPP)-grafted β -CD-modified hyaluronic acid (TPP-HACD), disulfide bond-linked permethyl- β -CD-camptothecin prodrug (PMCD-SS-CPT), and water-soluble adamantane-porphyrin photosensitizer (aPs), had several inherent advantages: (1) the prodrug PMCD-SS-CPT, where the permethyl- β -CD and CPT were bridged by a disulfide bond, was endowed with cancer microenvironment responsiveness for site-specific on-demand drug release; (2) water-soluble adamantane-modified porphyrin (aPs) was utilized as a photosensitizer, which showed extraordinary affinity with permethyl- β -CD (PMCD), thus eliminating self-quenching of aPs in an aqueous solution; (3) a biocompatible polysaccharide hyaluronic acid (HA) was decorated with triphenylphosphine (TPP) and β -CD for cancer-mitochondria dual-targeting because of the overexpressed CD44 receptors on the cancer cell surface; and (4) the nano-supramolecular assemblies could be simply constructed through the orthogonal host–guest interactions between PMCD and water-soluble porphyrin and β -CD and the adamantane. The obtained NPs could specifically accumulate in the mitochondria of A549 cancer cells, and chemo-photodynamic combinational therapy was performed to induce mitochondria-mediated apoptosis, thus realizing enhanced anticancer efficacy. Consequently, these results displayed the high-efficiency synergistic effect of supramolecular nano-

particles on cancer therapy, which provides a new therapeutic strategy for step-by-step combinational chemo-photodynamic therapy against cancer cells.

EXPERIMENTAL SECTION

Materials. All chemicals and solvents were commercially available and used as received without further purification unless noted otherwise. β -Cyclodextrin (β -CD) was recrystallized twice from water and dried in vacuo at 90 °C for 24 h prior to use. Anhydrous CH_2Cl_2 and dry DMF were dried over CaH_2 for 24 h and then distilled prior to use. The reaction was monitored using analytical thin layer chromatography (TLC, GF254). Column chromatography was performed on a 200–300 mesh silica gel.

Measurements. All the photophysical experiments were performed at 298 K in deionized water (pH = 7.2). ^1H NMR (400 MHz) and ^{13}C NMR (100 MHz) spectra were recorded on Bruker Avance spectrometers. The mass spectra of the compounds were recorded on Varian 7.0 T FTMS with the MALDI ion source and a Q-TOF LC-MS with an ESI mode. The white light irradiation experiment was carried out by employing a CEL-HXUV300 xenon lamp with a >420 nm cutoff filter at a power density of 220 mW/cm². UV–vis spectra were recorded on a Shimadzu UV-3600 spectrophotometer with a PTC-348WI temperature controller in a quartz cell (light path 10 mm) at 25 °C. Steady-state fluorescence spectra were measured in a quartz cell (light path 10 mm) using a Varian Cary Eclipse fluorescence spectrometer at 25 °C with a constant-temperature water bath. Induced circular dichroism spectra were collected on a BioLogic MOS500 spectropolarimeter in a quartz cell (light path 10 mm). For dynamic light scattering (DLS) measurements, the sample solution (3 mL) was filtered through a 0.45 μm Millipore filter and then examined on a laser light-scattering spectrometer (BI-200SM) equipped with a digital correlator (Turbo Corr) at 636 nm at a scattering angle of 90°. Zeta potential analysis was performed on a Brookhaven ZetaPALS (Brookhaven Instrument, USA) at 298 K in H_2O . The TEM images were recorded by a high-resolution transmission electron microscope (Philips Tecnai G2 20S-TWIN microscope) operating at an accelerating voltage of 200 keV. The SEM images were recorded on a JEOL JSM-7500F scanning electronic microscope operating at an accelerating voltage of 30 keV. For AFM measurements, the sample solution was dropped onto newly clipped mica and air dried, and the residue obtained was examined in the air under ambient conditions using a Veeco Nano IIIa Multimode AFM instrument. The fluorescent confocal images were carried out on a Leica TCS SP8 fluorescence microscope.

Preparation and Drug Loading Content (DLC)/Encapsulation Efficiency (EE) of Nanoparticles (NPs). Compound 3 (0.94 mg, 1 mmol) was first neutralized with NaOH to directly afford the water-soluble anionic porphyrin in deionized water (1 mL) according to the literature.³⁵ Then PMCD-SS-CPT (4.41 mg, 2 mmol) was added to the solution and mixed well. After that, TPP-HACD (5.76 mg, containing 1.5 mmol β -CD to ensure sufficient binding) was added into the abovementioned solution followed by ultrasound until completely dissolved. The resulting solution was subsequently subjected to dialysis (MWCO 3500) against excess amount of deionized water for 24 h at room temperature to remove any unbound components and was further stored in the refrigerator at 4 °C for further use. The morphology and size of the nanoparticles were characterized by TEM, SEM, AFM, and DLS studies. The drug loading content (DLC) and encapsulation efficiency could be calculated from the following formulas (eqs 1 and 2):

$$\text{drug loading content (\%)} = 100 \times \frac{W_{\text{drug in nanoparticles}}}{W_{\text{nanoparticles}}} \quad (1)$$

$$\text{encapsulation efficiency (\%)} = 100 \times \frac{W_{\text{drug in nanoparticles}}}{W_{\text{total drug}}} \quad (2)$$

The concentration of loaded PMCD-SS-CPT was measured by UV-vis spectra and a standard curve plotted by the absorbance at 369 nm.

In Vitro Drug-Releasing Study. The drug-release performance of the supramolecular nanoparticles (NPs) was investigated in phosphate buffer solution (PBS, pH 7.2). Briefly, 2 mL of NP solution (3 mg/mL) was placed in a dialysis tube (MWCO 3500) at 37 °C. Then, the dialysis tube immersed in 25 mL of PBS solution containing 1 or 10 mM GSH at 37 °C. At predetermined time intervals, 3 mL of the release medium was sampled and replaced by another 3 mL of fresh PBS. The amount of released drug outside the dialysis bag from the NPs was determined by a UV-vis spectrometer.

Cell Culture. Human lung cancer A549 cell line and human embryonic kidney 293T cell line were obtained from Institute of Basic Medical Science, Chinese Academy of Medical Science. A549 cells were cultured in a cell incubator with Ham's F12 nutrient medium containing 10% fetal bovine serum and 1% penicillin-streptomycin under 5% CO₂ at 37 °C. Additionally, 293T cells were cultured in a cell incubator with a DMEM high-glucose nutrient medium containing 10% fetal bovine serum and 1% penicillin-streptomycin in a humidified standard under 5% CO₂ at 37 °C.

Cell Uptake and Colocalization Imaging. A549 cells were seeded onto a laser confocal Petri dish and cultivated for 24 h. Then, the NPs were added into the dish and incubated with the cells for different durations of 2 and 4 h. Finally, the cells were washed thoroughly with PBS (0.01 M) three times and observed via CLSM (excitation filter: 405 nm; emission: 620–750 nm). A549 cells were seeded onto a laser confocal Petri dish and cultivated for 24 h. The NPs were added into the dish and incubated for 12 h. Afterward, the culture medium was removed and washed with PBS (0.01 M) three times. Subsequently, MitoTracker Green was added to stain the mitochondria at 37 °C for 30 min. After repeated washing with PBS three times, the cells were observed directly via CLSM. For MitoTracker Green, the excitation filter was 488 nm, and the emission was 510–540 nm. For NPs, the excitation filter was 405 nm, and the emission was 620–750 nm.

Extracellular ROS Detection. 9,10-Anthracenediyl-bis-(methylene)dimalonic acid (ABDA) as a chemical probe was employed to confirm the ROS production of NPs. In the experiments, 20 μL of ABDA (0.01 M DMSO) stock solution was mixed with 3 mL of NPs in deionized water and then exposed to the white light (220 mW/cm²) at different intervals. The ¹O₂ generation was detected by a UV-vis spectrometer through monitoring the change in absorbance of ABDA at around 378 nm at various irradiation times. The ¹O₂ generation of NPs was also detected by using TEMP as a ¹O₂ trapping agent for ESR measurement. Briefly, the NPs (0.1 mM) were exposed to white light irradiation (220 mW/cm²) for 10 min in the presence of TEMP (1 mM). Then, the ¹O₂ signal was then observed as soon as possible via an ESR spectrometer.

Intracellular ROS Detection. The intracellular generation of ¹O₂ was also detected by 2',7'-dichlorofluorescein diacetate (DCFH-DA), a commercially available singlet oxygen indicator, which could be converted to DCF that exhibited brightly emissive green fluorescence in the presence of ¹O₂. Typically, the cells were incubated with NPs (10 μM) for 12 h. After that, the cells were washed with PBS (0.01 M) three times and fresh culture medium containing 20 μM 2',7'-dichlorofluorescein diacetate (DCFH-DA) was added followed by incubation for 30 min, one of which that was pretreated with vitamin C (50 μM) for 10 min was used as a control. Then, the cells were washed with PBS (0.01 M) three times again and irradiated by white light (white light, 220 mW/cm², 10 min). The cells were then observed as soon as possible via CLSM. The excitation wavelength was 488 nm, and the collection wavelength range was from 510 to 540 nm.

Cell Cytotoxicity. A549 cells were seeded into a 96-well plate and then treated with different concentrations of NPs. The final concentration of NPs was 10, 8, 6, 4, and 2 μM, respectively. Then, the cells were incubated with NPs in the dark for 24 h. After that, the white light irradiation (220 mW/cm²) was applied for 10 min. Then, the cells were continuously cultured for another 1 h. The cell viability

was evaluated by CCK8 assay according to the kit instruction. The plate was then read by a microplate reader at a wavelength of 450 nm. All the data were presented as the mean ± standard deviation. NPs without CPT were produced by using PMCD instead of PMCD-SS-CPT for preparation and used as the control group. The NP concentrations were calculated based on the aPs concentration.

Live/Dead Cell Assay. A commercial calcein-AM/PI assay kit was directly used according to the kit instruction. The cells were treated in the same ways as above and co-stained with calcein-AM and propidium iodide (PI) for 30 min. Then, the cells were washed with PBS (0.01 M) three times to remove excess staining reagents. The cells were then observed immediately via CLSM. For these two reagents, they were all excited at 488 nm, and the collection wavelength range was from 520 to 530 nm for calcein-AM and from 610 to 640 nm for PI.

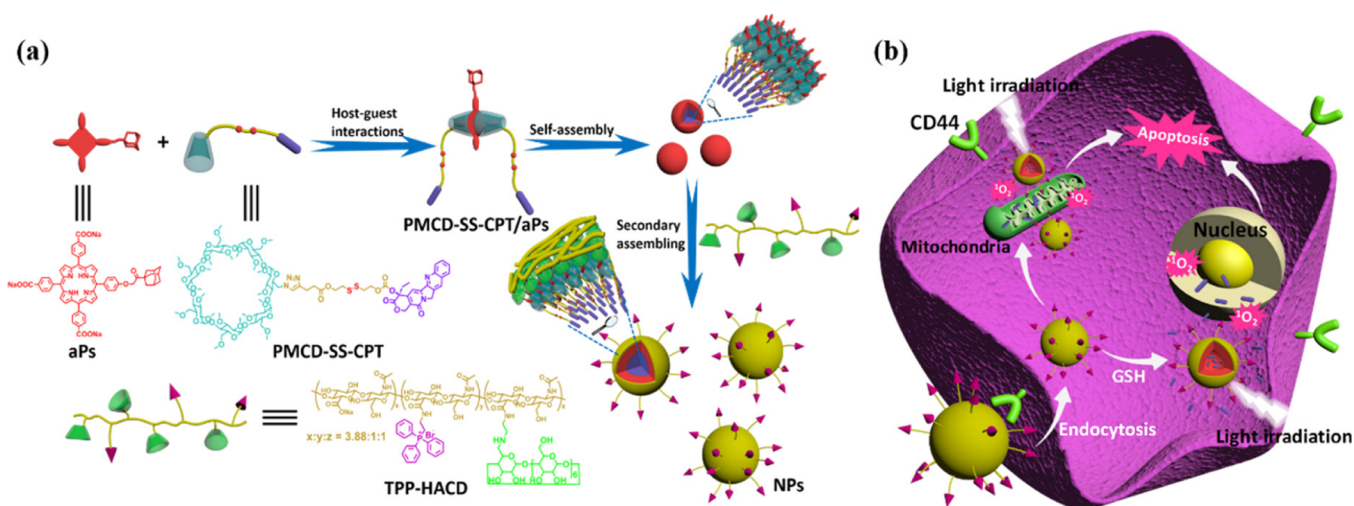
JC-1 Staining Assay. The decrease in mitochondrial membrane potential could be distinguished sensitively by the difference in red/green fluorescence intensity. The probe tended to enter the mitochondrial matrix forming J-aggregates to produce red fluorescence when the mitochondrial membrane potential was high, whereas it could only exist in the cytoplasm as a monomer producing green fluorescence when the mitochondrial membrane potential was lost. The cells were treated in the same ways as above and stained with JC-1 for 30 min. Then, the cells were washed with PBS (0.01 M) three times to remove excess staining reagents. The cells were then observed immediately via CLSM. They were all excited at 488 nm, and the collection wavelength range was from 520 to 530 nm for the JC-1 monomer and from 610 to 640 nm for the JC-1 aggregate.

Apoptosis Study. A549 cells were seeded into a 6-well plate and cultured at 37 °C for 24 h. Then, the cells were co-incubated with NPs (5 μM) in the dark for 24 h. Afterward, the cells were treated under different conditions. The adherent cells were harvested with trypsin first, then washed with PBS, dispersed in 100 μL of binding buffer, stained with annexin VFITC/PI for 10 min at room temperature and protected from light, and then immediately detected by flow cytometry.

RESULTS AND DISCUSSION

Synthetic routes to the target molecules are outlined in Scheme S1–S3, respectively. The obtained compounds were comprehensively characterized by ¹H and ¹³C NMR spectra, and ESI-MS spectroscopies were consistent with their devised structures (Figures S1–S10). In brief, the water-soluble adamantane-modified anionic porphyrin ADA-Porphyrin (aPs) was obtained from 5,10,15-tris(4-methoxycarbonylphenyl)-20-(4-hydroxyphenyl)porphyrin (2) by reacting with 1-adamanyl bromomethyl ketone (1) in the presence of K₂CO₃, then the intermediate was hydrolyzed and further neutralized with equivalent NaOH to directly afford the desired compound.³⁵ The alkynyl-substituted CPT was synthesized according to the reported literature with a slight modification. Subsequently, the intermediate reacted with excess 6-deoxy-6-azido-permethyl-β-CD in the presence of CuI via the Huisgen 1,3-dipolar cycloaddition to give PMCD-SS-CPT in 52% yield. As shown in Figure S5, a typical proton signal at 7.45 ppm was assignable to the triazole ring, proving the successful connection of CPT and PMCD. The triphenylphosphonium cations (TPP) and β-CD-modified TPP-HACD were prepared by means of one-step amide condensation between sodium hyaluronate (HA) with (PPh³⁺(CH₂)₂NH₂)Br⁻ and mono-6-deoxy-6-ethylenediamino-β-CD in phosphate buffer solution (PBS). The substitution degrees of triphenylphosphonium and β-CD attached to HA were determined by comparing the integral area of the H₁ proton of β-CD at 5.04 ppm and the H_{ph} proton of TPP at 7.57–7.94 ppm with that of the *N*-acetyl

Scheme 1. Schematic Illustration of the (a) Formation of NPs and (b) Their Application for Synergistic Chemo-photodynamic Cancer Therapy



protons of HA at 1.98 ppm, which were calculated as 17.0 and 17.1%, respectively.

The host–guest properties between PMCD-SS-CPT and aPs were first studied by UV–vis spectroscopy. The complexation stoichiometry between PMCD and aPs was determined as 2:1 by Job analysis in which the maximum exhibited a peak at a molar fraction around 0.33 when PMCD was employed as a reference host (Figure S11). Moreover, the binding constants (K_s) between PMCD-SS-CPT and aPs were calculated as $K_1 = 1.1 \times 10^8 \text{ M}^{-1}$ and $K_2 = 2.3 \times 10^7 \text{ M}^{-1}$ from the UV–vis spectral titration data through analyzing the sequential changes in absorbance intensity (ΔA) at varying concentrations of PMCD-SS-CPT by using a nonlinear least-squares curve-fitting method (Figure S12). The obtained K_s were similarly consistent in the previous reported literature.^{36–38} The strong binding made it particularly easy to construct supramolecular assemblies PMCD-SS-CPT/aPs upon mixing PMCD-SS-CPT and aPs in aqueous solution. Meanwhile, as shown in Figure S12a, the broadened Soret band of aPs gradually became sharper accompanied by a bathochromic shift from 412 to 416 nm upon stepwise addition of PMCD-SS-CPT. In addition, aPs showed a relatively low intensity in aqueous solution, probably due to the amphiphilic structure of aPs, which made it easy to form H-aggregates in aqueous solution. However, the fluorescence intensity of aPs was greatly enhanced after addition of PMCD-SS-CPT, indicating that PMCD-SS-CPT prevented intermolecular aggregation between aPs by forming a stable supramolecular PMCD-SS-CPT/aPs complex (Figure S13). Moreover, the additional evidence coming from the circular dichroism (CD) spectroscopy confirmed the non-covalent association between aPs and PMCD-SS-CPT. As exhibited in Figure S14, relatively high circular dichroism signals were observed in the Soret band of aPs from the circular dichroism spectrum upon the addition of PMCD-SS-CPT, whereas free aPs presented almost no appreciable circular dichroism signals at the same wavelength. PMCD-SS-CPT also exhibited well-defined circular dichroism signals from 300 to 400 nm, resulting from the inherent chiral property in the camptothecin molecule. Therefore, these phenomena jointly suggested the formation of a PMCD-SS-CPT/aPs complex in aqueous solution. The complexation between aPs and PMCD-SS-CPT was further characterized by

NMR spectroscopy. For the PMCD-SS-CPT/aPs complex, as could be seen from the 2D NOESY spectrum (Figure S15), the phenyl protons of aPs at 7.0–9.0 ppm presented distinct multiple cross-peaks with the PMCD of the secondary OCH_3 , indicating that the porphyrin moiety of aPs could be included completely into the cavity of PMCD. Combined with the above experimental results, we could confirm the satisfactory complexation between aPs and PMCD-SS-CPT.

Owing to the amphipathic structure of PMCD-SS-CPT and the strong bonding ability between aPs and PMCD, the assembly behavior of PMCD-SS-CPT in the presence or absence of aPs was explored. As shown in Figure S16, a series of spherical-shaped nanoparticles with an average diameter ranging from 10 to 20 nm were observed in a typical TEM image. Meanwhile, PMCD-SS-CPT/aPs could self-assemble into a bit larger nanoparticles whose diameters are distributed from 30 to 40 nm in aqueous solution. To further confirm the self-assembly process, the critical micelle concentration (CMC) value of PMCD-SS-CPT/aPs was investigated by monitoring the change in optical transmittance at different concentrations of the complex. As shown in Figure S17, the optical transmittance of PMCD-SS-CPT/aPs at 514 nm displayed no obvious change when the concentration of the complex increased from 0 to 1.5 μM , whereas the optical transmittance gradually decreased with increasing concentration of the complex from 1.65 μM indicative of the formation of aggregates. The possible assembly modes are shown in Scheme 1.

After successful preparation and characterization of the binary assembly, TPP-HACD was introduced for ternary assembly benefiting from the highly affiliative interactions between adamantane and β -CD.^{39–41} Thus, a hierarchical supramolecular nanoparticle TPP-HACD@PMCD-SS-CPT/aPs (NP) composed of TPP-HACD, PMCD-SS-CPT/aPs could be easily constructed by conveniently mixing these abovementioned components in aqueous solution. The size and morphology of the obtained nanoparticles were fully investigated by high-resolution transmission electron microscopy (HR-TEM), scanning electron microscopy (SEM), atomic force microscopy (AFM), dynamic light scattering (DLS), and zeta potential experiments. As shown in Figure S18, the fluorescence intensity of PMCD-SS-CPT/aPs

displayed negligible change when TPP-HACD was added, implying that the TPP-HACD could not disturb the association between PMCD-SS-CPT and aPs because of their highly extraordinary binding affinity. For another, the free TPP-HACD was mainly observed as the loose and amorphous structure that was easy to aggregate (Figure S19a). However, the HR-TEM images revealed that a majority of these ternary nanoparticles almost existed as homogeneous spheres with an average diameter of 100 nm (Figure 1b),

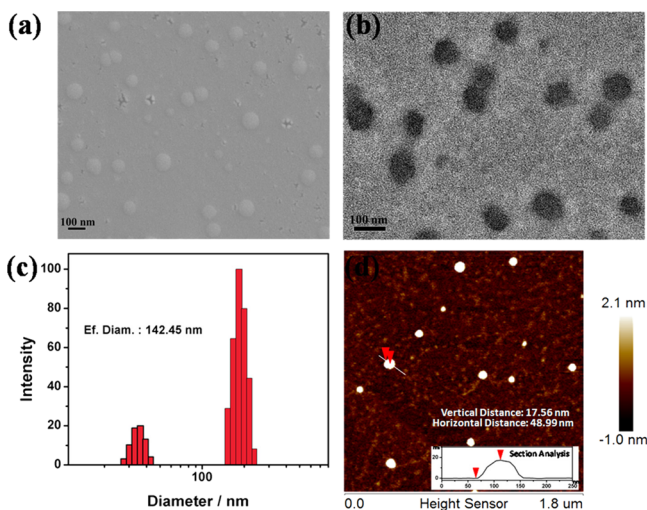


Figure 1. Typical (a) SEM, (b) HR-TEM, and (d) AFM images of NPs. (c) DLS result of NPs.

which were a much larger assembly than PMCD-SS-CPT/aPs and more uniform than free TPP-HACD, indicating the formation of the ternary nanoparticles. Additionally, these

nanoparticles were slightly inclined to aggregate influenced by the hydrogen bonding interactions among the abundant carboxylic and hydroxyl groups on the backbone of HA. This phenomenon was also verified by SEM images (Figure 1a), which displayed the similar morphological information with TEM, showing many spherical nanoparticles whose diameter was around 100 nm. Subsequently, a number of collapsed nanoparticles with spherical shape were found in AFM images (Figure 1d) as well, whose height was measured as about 10 nm, and its diameter was determined from 80 to 100 nm, which was in fine accordance with the results above. Moreover, DLS data showed that NPs possessed an average hydrodynamic diameter of 142.45 nm (Figure 1c), which were appreciably larger than that observed in TEM images, due to the shrinking of nanoparticles upon air drying in the sample preparation for TEM. It was worth noting that DLS presented a signal with a hydrodynamic diameter around 30 nm, which was probably attributed to the dynamic reversible properties of supramolecular interactions. In the control experiment, the hydrodynamic diameter of TPP-HACD was determined up to thousands of nanometers according to the DLS results on account of its own aggregated feature (Figure S19b). Furthermore, the zeta potential of NPs was measured as -10.33 mV (Figure S20b) due to the distribution of negatively charged hydrophilic TPP-HACD on the surface, indicating that TPP-HACD served as the shell of the nanoparticle. This was in sharp contrast with PMCD-SS-CPT whose zeta potential was measured as -0.62 mV (Figure S20a), demonstrating its uncharged surface. The possible assembly mode of NPs is illustrated in Scheme 1. PMCD-SS-CPT/aPs and TPP-HACD coassembled to small micelles first, and a hydrophilic TPP-HACD backbone was considered as the outer shell of these small micelles. Subsequently, these small micelles further aggregated to form larger nanoparticles through

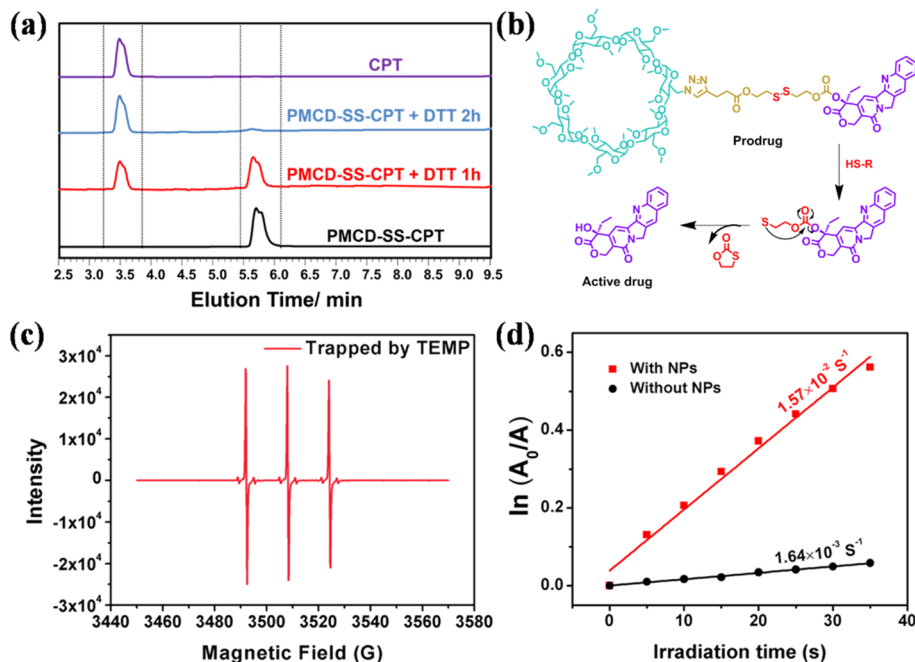


Figure 2. (a) HPLC analysis of PMCD-SS-CPT upon treatment with DTT at varying time durations. The absorption channel was set at 254 nm ($[PMCD-SS-CPT] = 0.1$ mM). (b) Proposed mechanism of CPT drug release from reduction-responsive prodrug PMCD-SS-CPT. (c) Electron spin resonance (ESR) spectra of NPs ($[NPs] = 0.1$ mM) with serving TEMP as the spin trap. Irradiation time is 10 min. (d) Decomposition rate of ABDA at 378 nm versus different irradiation times; A_0 is the original absorption of ABDA, and A is the absorption with different irradiation times.

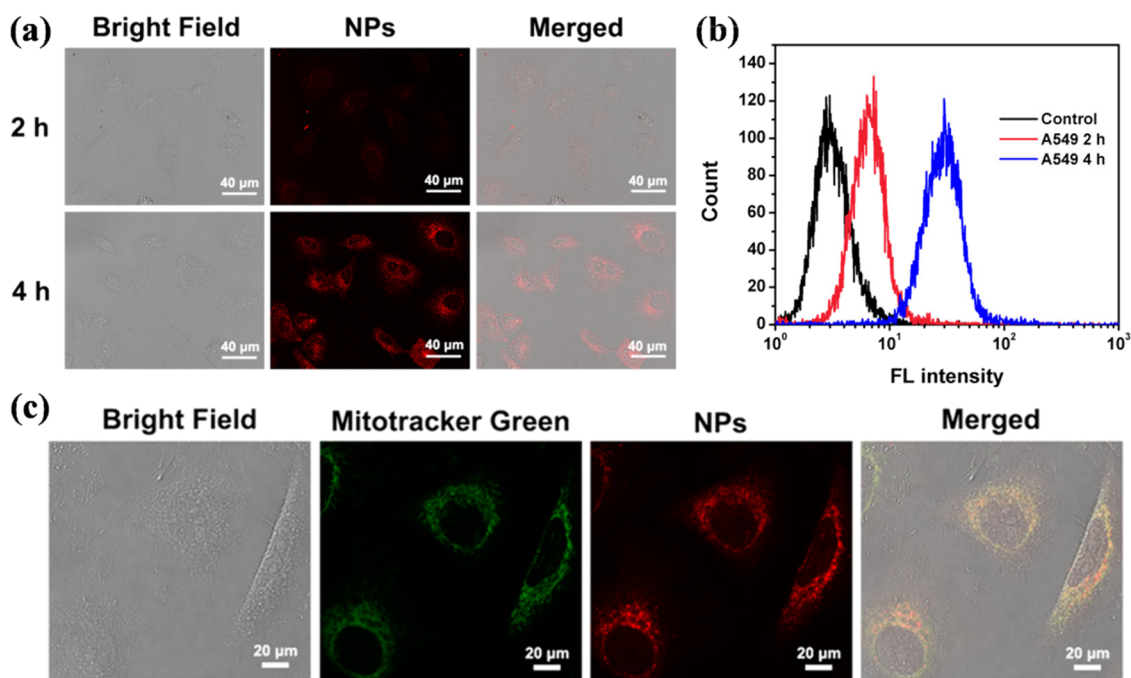


Figure 3. (a) Confocal laser scanning microscopy images of time-dependent cellular uptake of A549 cells when incubated with NPs (5 μM) for different incubation times (2 and 4 h). (b) Flow cytometric analysis of A549 cells in panel (a), and the black lines represented the untreated control cells. (c) Mitochondria-specific subcellular colocalization experiments in living A549 cells.

supramolecular interactions such as hydrogen bonding interactions of carboxylic and hydroxyl groups in TPP-HACD via the small micelle aggregation mechanism or multi-compartment micelle formation mechanism.^{36,42} In addition, the NP zeta potential value was slightly smaller than the HA-based assembly, previously reported in the literature,^{43,44} probably due to the modification of the TPP moiety that neutralized some negative charge of the HA backbone. The negatively charged surface endowed the obtained ternary NPs with more favorable characteristics such as improved targeting property, good biocompatibility, and stability in biological environments.

Furthermore, the successful preparation of nanoparticles could also be identified by the naked eyes. As shown in Figure S21, the NPs appeared as clear and transparent solution accompanied by an obvious pink color coming from aPs in daylight. Meanwhile, the solution of NPs showed a more apparent Tyndall effect than that of TPP-HACD alone, further confirming the formation and existence of nanoparticles. Moreover, the solution of NPs was still steady without precipitation and exhibited a clear Tyndall effect even after being allowed to stand for 1 month, implying the favorable stability of nanoparticles. In addition, the drug loading content (DLC) and the encapsulation efficiency (EE) were determined to be 36.2 and 97.5% according to the standard curve of PMCD-SS-CPT, respectively (Figure S22), which was comparable to the previous reports of supramolecular assemblies based on a prodrug.^{45,46}

To investigate the CPT release ability of PMCD-SS-CPT responding to reductivity, high-performance liquid chromatography (HPLC) was utilized to detect the cleavage of the disulfide bond at different intervals by co-incubation with model thiol that triggers dithiothreitol (DTT).⁴⁷ As shown in Figure 2a, for PMCD-SS-CPT, a peak whose retention time at 5.7 min in the HPLC chromatogram was monitored, while no

CPT release was detected in the absence of DTT. However, in contrast, after incubating PMCD-SS-CPT with 10.0 mM DTT for 1 h, a new peak corresponding to CPT at 3.5 min appeared obviously. As expected, the peak intensity of CPT increased gradually accompanied by diminishing the peak of PMCD-SS-CPT with the prolonging of incubation time. PMCD-SS-CPT was almost completely converted into CPT after 2 h of incubation, indicating its favorable GSH responsiveness. The proposed mechanism of CPT from reduction-responsive PMCD-SS-CPT is shown in Figure 2b. These results confirmed that the synthesized prodrug could indeed release the active CPT through a GSH-responsive release mode. The TEM images (Figure S23) also demonstrated that the NPs would dissociate into shapeless aggregates after treating the NPs with DTT for 4 h, manifesting that the NPs exhibited a high response toward reducing agents. Moreover, the drug-releasing behavior of NPs was further studied by the dialysis method. As shown in Figure S24, the amount of released drug increased when increasing the concentration of the reducing agent GSH. No apparent drug release was observed when incubating without GSH. However, treatment with 1 mM GSH led to 45% drug release from the NPs after 24 h. In comparison, higher concentration of GSH at 10 mM accelerated drug release with 80% during the same period. These experimental results consistently indicated the good drug-releasing characteristics of supramolecular nanoparticles in a mimetic tumor microenvironment.

Next, to assess the ability of the assembly generating singlet oxygen (¹O₂), TEMP, a commercially available spin-trapping agent of ¹O₂ was employed for electron spin resonance (ESR) experiments to characterize their adduct TEMP-¹O₂.⁴⁸ As presented in Figure 2c, a unique three-line signal, accompanied with a hyperfine coupling constant of 16.0 G and an intensity ratio of 1:1:1 from the adduct of ¹O₂ and TEMP, was observed in the ESR spectrum upon irradiation with white light. To

further verify the formation of $^1\text{O}_2$, the common singlet oxygen detecting agent 9,10-anthracenediylbis(methylene)dimalonic acid (ABDA) was chosen to detect the ROS generation of NPs in solution under white light irradiation or not. ABDA was usually adopted as an indicator of the generation of $^1\text{O}_2$ since $^1\text{O}_2$ was a sensitive destructor of the conjugated unit of anthracene in ABDA. As illustrated in Figure S25, the absorbance of ABDA had almost no decrease with the extension of illumination time, which proved the stability of this compound under this light intensity. However, in the presence of NPs, something dramatically different was that the absorbance of ABDA gradually decreased with the lighting time increased, confirming that NPs could indeed produce $^1\text{O}_2$ upon the exposure to light, and the decomposition rate of ABDA was measured as $1.57 \times 10^{-2} \text{ S}^{-1}$ (Figure 2d). In addition, the NPs exhibited good photostability in aqueous solution, which was beneficial for further biological applications. These experiments all demonstrated that the NPs could be utilized as an excellent singlet oxygen generator in aqueous solution under light irradiation, which was beneficial for PDT.

After fully characterizing NPs and verifying their responsive drug-release capacity and $^1\text{O}_2$ generation ability, the intracellular accumulation of NPs was observed by confocal laser scanning microscopy (CLSM). The results showed that the uptake of NPs into the cell exhibited a time-dependent manner (Figure 3a). After 2 h of co-cultivation, there was an exhibited weak red fluorescence in the cancer cells, indicating a little uptake of the NPs. As the co-cultivation time increased to 4 h, the NPs were almost distributed in the cytoplasm monitored by the bright red fluorescence originated from aPs, suggesting the accumulation of NPs in cells. The flow cytometric analysis further confirmed this result (Figure 3b). In addition, the blue fluorescence arising from CPT was also found in the cytoplasm (revealed by Figure S26). Thus, these phenomena consistently indicated that the assembly NPs could be efficiently taken up by A549 cells. Subsequently, the cellular uptake mediated by HA toward different cell lines of NPs was evaluated. As shown in Figure S27, the A549 cells exhibited bright red fluorescence after the incubation with NPs, while negligible fluorescence was observed in 293T cells due to the lack of a CD44 receptor on the cell surface. These phenomena indicated that the CD44 receptor-mediated endocytosis effect played an important part in the internalization of the NPs, and the introduction of HA could distinctly bring down the cellular uptake of NPs into normal cells. Additionally, given that the mitochondrial targeting unit triphenylphosphonium cation was attached to nanoassembly surfaces, it was supposed to promote the NP accumulation in the mitochondria. The intracellular colocalization analysis of NPs and MitoTracker Green was exhibited in A549 cells. As shown in Figure 3c, the red fluorescence of NPs was overlapped well with the fluorescence of MitoTracker Green, and the Pearson's correlation was determined as high as 0.70, demonstrating the specific mitochondria-targeting ability of NPs.

To further monitor the intracellular generation of $^1\text{O}_2$, the real-time confocal microscopy was performed to observe the cell injury under continuous laser irradiation. As shown in Figure 4a, significant characteristics of cell apoptosis such as membrane blebbing and morphology change of the nucleus could be visualized when the cells treated with NPs were irradiated. In the controlled experiment, the cell under only laser irradiation still maintained its structural integrity and stability, proving that the bubbles were indeed caused by the

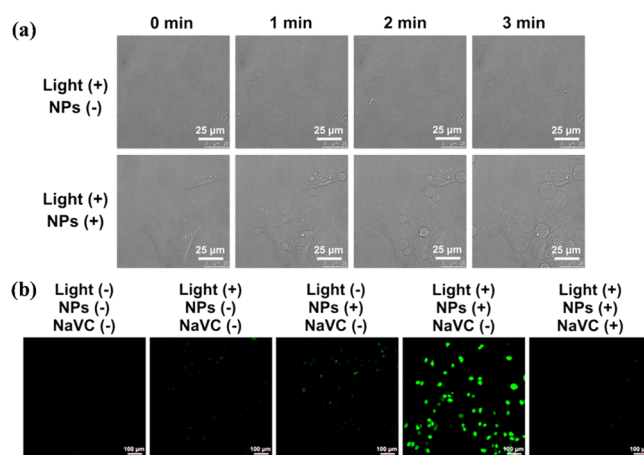


Figure 4. (a) Real-time confocal imaging of A549 cells under continuous 405 nm laser irradiation treated with or without NPs. The scale bar represents 25 μm . (b) Intracellular $^1\text{O}_2$ detection in A549 cells using a DCFH-DA enzyme under different treatments. NaVC was utilized as a $^1\text{O}_2$ scavenger.

$^1\text{O}_2$ produced by NPs rather than local overheating caused by laser irradiation. The intracellular $^1\text{O}_2$ level was also visualized by using a commercial available singlet oxygen indicator 2',7'-dichlorofluorescein diacetate (DCFH-DA). As illustrated in Figure 4b, strong green fluorescence was observed in cells cultured with NPs followed by light irradiation, confirming the production of a large amount of $^1\text{O}_2$, while weak green fluorescence was detected when cells were treated with NPs only. Moreover, almost no green fluorescence was observed in other groups for both in dark and under light without NP treatment. In addition, after being treated with vitamin C, a common reactive oxygen scavenger,⁴⁹ the cells exhibited weak green fluorescence, further demonstrating the intracellular generation of $^1\text{O}_2$.

Subsequently, the cytotoxicity experiment was evaluated by using a standard cell counting kit-8 (CCK-8) assay in order to investigate the combinational anticancer activities of NPs. As shown in Figure 5a, cell viability of A549 cells hardly declined after the cells were treated with the control samples for 24 h, implying its low cytotoxicity in the dark. However, the NPs displayed higher cytotoxicity under the same conditions, which was attributed to the CPT release activated under GSH, thus inducing cell death and showing the 41% inhibition of tumor cell proliferation at the concentration of NPs as 10 μM . Notably, the treatment with NPs followed by light irradiation exhibited the most remarkably substantial suppression on cell viability owing to the photosensitization of aPs producing $^1\text{O}_2$. The viability of tumor cells decreased rapidly about 80% when the concentration of NPs reached 10 μM , implying the conspicuous synergistic anticancer effect of NPs. Moreover, the synergistic effect of NPs was quantitatively evaluated by the combination index (CI) values.⁵⁰ As described in Figure S28, the CI values of NPs toward A549 cells were all determined to be less than 1 in the range from IC_{30} to IC_{70} , demonstrating the PMCD-SS-CPT prodrug and aPs within NPs exhibited a synergistic effect during the therapy process. Additionally, A549 cells still maintained a high cell survival rate (more than 95%) after being co-cultured with Ph₃P-HACD for 24 and 48 h, demonstrating the low toxicity and good biocompatibility of the HA backbone (Figure S29). Furthermore, flow cytometry analysis was performed to quantitatively discern the apoptotic

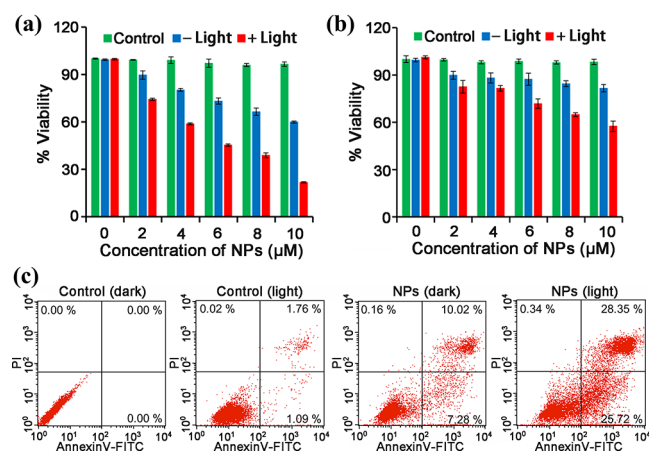


Figure 5. In vitro cell viability of (a) A549 cells and (b) 293T cells after 24 h of treatment with NPs in the absence or presence of light irradiation at different concentrations. The concentrations were calculated based on aPs concentration. (c) Cell apoptosis and necrosis of A549 cells analyzed by a flow cytometer with annexin V-FITC/PI dual staining after treatment with (a) control, (b) light irradiation alone, (c) NPs, and (d) NPs + light irradiation ($[NPs] = 5 \mu M$).

and necrotic cells at different stages by the annexin V-FITC/PI dual-staining method. As illustrated in Figure 5c, no significant cell necrosis was observed in all groups accompanied with the cell necrosis rate less than 0.4%. The cells only treated with light irradiation displayed the relatively low apoptosis rate 2.83%, proving that the light irradiation did little discernible damage to the cells. Nevertheless, after being treated with NPs at a concentration of $5 \mu M$, the apoptosis rate of A549 cells was determined as 17.19%. Moreover, after the treatment with NPs and light irradiation, the population of apoptosis cells reached 53.10%, which was much higher than that of other treatment groups and in accordance with the CCK-8 results. Additionally, the cell apoptosis was induced by both early and late apoptosis, while the late apoptosis rate was slightly higher than the early apoptosis. These results strongly indicated the applicability of NPs as a promising efficient reagent in the presence of light for step-by-step synergistic cancer therapy.

In addition, the cytotoxicity of NPs toward 293T normal cells was also investigated. As shown in Figure 5b, compared with A549 cancer cells, NPs all exhibited relatively higher cellular viability in the presence or absence of light. The cell viability of 293T cells was measured as 57% after being treated with NPs ($10 \mu M$) and light irradiation, which was significantly higher than the corresponding value for cancer cells. Combining the confocal fluorescence images in Figure S25 and cytotoxicity experiments, these results jointly indicated that the obtained NP assembly exhibited specific targeting and selective accumulation ability in cancer cells and released the active drug because of the overexpressed GSH in cancer cells. Therefore, the NPs could serve as an efficient and safe therapeutic reagent to kill cancer cells while exhibiting less damage toward normal cells, thus reducing side effects of classical chemotherapy and PDT.

The combinational therapy efficacy of NPs was also verified by live/dead cell co-staining experiment. As shown in Figure 6, a completely strong green fluorescence together with no red fluorescence was found in A549 cells without any treatment, and the same result was observed in cells treated with light alone, proving that the cells stayed alive entirely under these

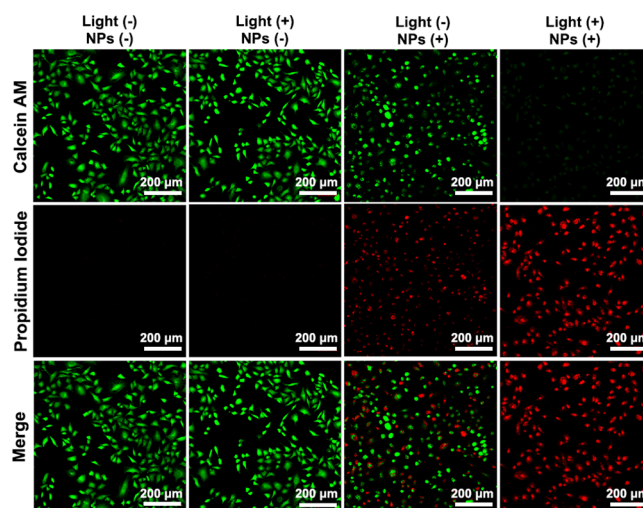


Figure 6. Confocal laser scanning microscopy images of calcein AM and propidium iodide co-staining on A549 cells upon different treatments. Live/dead cells were stained green/red with calcein AM/PI, respectively.

conditions. In contrast, a significant number of the cells were killed in the presence of NPs as revealed by the red fluorescence from nuclei stained by PI and the relatively weak green fluorescence compared with the former two groups, which was caused by the release of CPT from the NPs on account of the excess GSH in cancer cells. Significantly, only intense red fluorescence and negligible green fluorescence were observed for NPs in the presence of the light, indicating their higher cellular toxicity and effective two-step synergistic therapy effect to A549 cells. These results suggested that NPs exhibited the most cytotoxic toward A549 cells after the two-step treatment, which were consistent with the toxicity tests.

Since NPs could accumulate in the mitochondria, we speculated that the released drugs and the produced 1O_2 from NPs could destroy the integrity of the mitochondrial membrane and further induce cell apoptosis. To investigate the damage caused to mitochondria during synergistic treatment, JC-1, a commercial mitochondrial membrane potential kit, was employed as a fluorescent probe to detect the mitochondrial changes in cells. As depicted in Figure 7, the light irradiation had almost no effect on the mitochondrial membrane potential

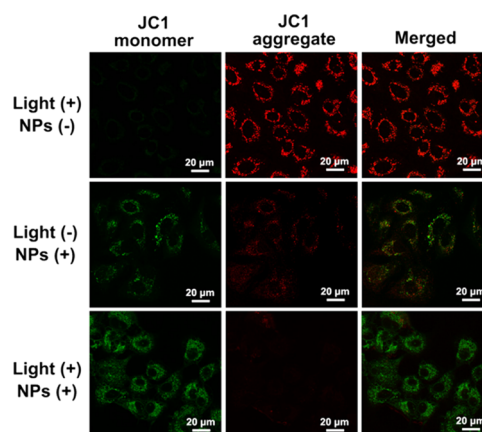


Figure 7. Mitochondrial membrane potential of A549 cells stained with JC-1 for visualizing the damage of mitochondria.

indicated by the strong red fluorescence. In contrast, severe mitochondrial depolarization was observed when incubated with NPs for 24 h as reflected by the enhanced green/red fluorescence intensity. Significantly, only green fluorescence was found in the presence of NPs followed by light irradiation, and mitochondria lost their normal morphological characteristics, suggesting the most serious mitochondrial membrane damage and mitochondrial dysfunction. This result further demonstrated that the synergistic treatment of NPs could damage the mitochondria seriously and then induced cell apoptosis eventually.

CONCLUSIONS

In summary, a cyclodextrin-prodrug supramolecular assembly with cancer-mitochondria dual-targeting property was successfully constructed by incorporating a prodrug, photosensitizer and TPP-HACD through an orthogonal host-guest recognition strategy to augment combinational chemotherapy and PDT for efficient step-by-step cancer treatment. These assemblies with suitable size could specifically target the mitochondria of cancer cells and release active drug CPT due to the cleavage of the disulfide bond under overexpressed GSH in cancer cells. Cytotoxicity experiments indicated that these assemblies exhibited much lower cytotoxicity toward normal cells than cancer cells in virtue of CD44 receptor-mediated endocytosis. The most severe mitochondrial dysfunction and cell death were demonstrated when tumor cells were incubated with NPs under light irradiation due to the synergistic chemotherapy of programmable CPT release and PDT deriving from light-triggered ROS generation. We believe the present studies may provide a novel strategy for the design and development of intelligent nanoassemblies applied to efficient step-by-step cancer combinational therapy.

ASSOCIATED CONTENT

Supporting Information

The Supporting Information is available free of charge at <https://pubs.acs.org/doi/10.1021/acs.biomac.0c01181>.

Synthesis procedures of intermediates; ^1H NMR, ^{13}C NMR spectra, and ESI-MS spectra of intermediates; absorption spectra and emission spectra; confocal laser scanning microscopy images; and cell viability test (PDF)

AUTHOR INFORMATION

Corresponding Author

Yu Liu – Department College of Chemistry, State Key Laboratory of Elemento-Organic Chemistry, Nankai University, Tianjin 300071, China; orcid.org/0000-0001-8723-1896; Email: yuliu@nankai.edu.cn

Authors

Xianyin Dai – Department College of Chemistry, State Key Laboratory of Elemento-Organic Chemistry, Nankai University, Tianjin 300071, China

Bing Zhang – Department College of Chemistry, State Key Laboratory of Elemento-Organic Chemistry, Nankai University, Tianjin 300071, China

Weilei Zhou – Department College of Chemistry, State Key Laboratory of Elemento-Organic Chemistry, Nankai University, Tianjin 300071, China

Complete contact information is available at:

<https://pubs.acs.org/10.1021/acs.biomac.0c01181>

Notes

The authors declare no competing financial interest.

ACKNOWLEDGMENTS

This work was financially supported by the National Natural Science Foundation of China (grant nos. 21672113, 21772099, 21861132001, and 21971127).

REFERENCES

- (1) Zhou, J.; Yu, G.; Huang, F. Supramolecular chemotherapy based on host-guest molecular recognition: a novel strategy in the battle against cancer with a bright future. *Chem. Soc. Rev.* **2017**, *46*, 7021–7053.
- (2) Yu, G.; Chen, X. Host-Guest Chemistry in Supramolecular Theranostics. *Theranostics* **2019**, *9*, 3041–3074.
- (3) Ma, X.; Zhao, Y. Biomedical Applications of Supramolecular Systems Based on Host-Guest Interactions. *Chem. Rev.* **2015**, *115*, 7794–7839.
- (4) Chen, Y.; Huang, F.; Li, Z.-T.; Liu, Y. Controllable macrocyclic supramolecular assemblies in aqueous solution. *Sci. China: Chem.* **2018**, *61*, 979–992.
- (5) Cheng, H.-B.; Zhang, Y.-M.; Liu, Y.; Yoon, J. Turn-On Supramolecular Host-Guest Nanosystems as Theranostics for Cancer. *Chem* **2019**, *5*, 553–574.
- (6) Kang, Y.; Ju, X.; Ding, L.-S.; Zhang, S.; Li, B.-J. Reactive Oxygen Species and Glutathione Dual Redox-Responsive Supramolecular Assemblies with Controllable Release Capability. *ACS Appl. Mater. Interfaces* **2017**, *9*, 4475–4484.
- (7) de Vries, W. C.; Kudruk, S.; Grill, D.; Niehues, M.; Matos, A. L. L.; Wissing, M.; Studer, A.; Gerke, V.; Ravoo, B. J. Controlled Cellular Delivery of Amphiphilic Cargo by Redox-Responsive Nanocontainers. *Adv. Sci.* **2019**, *6*, 1901935.
- (8) Guo, D.-S.; Liu, Y. Supramolecular chemistry of p-sulfonatocalix-[n]arenes and its biological applications. *Acc. Chem. Res.* **2014**, *47*, 1925–1934.
- (9) Wang, Y.-X.; Guo, D.-S.; Duan, Y.-C.; Wang, Y.-J.; Liu, Y. Amphiphilic p-sulfonatocalix[4]arene as “drug chaperone” for escorting anticancer drugs. *Sci. Rep.* **2015**, *5*, 9019.
- (10) Liu, X.; Jia, K.; Wang, Y.; Shao, W.; Yao, C.; Peng, L.; Zhang, D.; Hu, X.-Y.; Wang, L. Dual-Responsive Bola-Type Supra-Amphiphile Constructed from Water-Soluble Pillar[5]arene and Naphthalimide-Containing Amphiphile for Intracellular Drug Delivery. *ACS Appl. Mater. Interfaces* **2017**, *9*, 4843–4850.
- (11) Chen, J.; Zhang, Y.; Meng, Z.; Guo, L.; Yuan, X.; Zhang, Y.; Chai, Y.; Sessler, J. L.; Meng, Q.; Li, C. Supramolecular combination chemotherapy: a pH-responsive co-encapsulation drug delivery system. *Chem. Sci.* **2020**, *11*, 6275–6282.
- (12) Mao, D.; Liang, Y.; Liu, Y.; Zhou, X.; Ma, J.; Jiang, B.; Liu, J.; Ma, D. Acid-Labile Acyclic Cucurbit[n]uril Molecular Containers for Controlled Release. *Angew. Chem., Int. Ed.* **2017**, *56*, 12614–12618.
- (13) Ding, Y.-F.; Wei, J.; Li, S.; Pan, Y.-T.; Wang, L.-H.; Wang, R. Host-Guest Interactions Initiated Supramolecular Chitosan Nanogels for Selective Intracellular Drug Delivery. *ACS Appl. Mater. Interfaces* **2019**, *11*, 28665–28670.
- (14) Geng, W.-C.; Sessler, J. L.; Guo, D.-S. Supramolecular prodrugs based on host-guest interactions. *Chem. Soc. Rev.* **2020**, *49*, 2303–2315.
- (15) Cheetham, A. G.; Chakraborty, R. W.; Ma, W.; Cui, H. Self-assembling prodrugs. *Chem. Soc. Rev.* **2017**, *46*, 6638–6663.
- (16) Samanta, S. K.; Moncelet, D.; Briken, V.; Isaacs, L. Metal-Organic Polyhedron Capped with Cucurbit[8]uril Delivers Doxorubicin to Cancer Cells. *J. Am. Chem. Soc.* **2016**, *138*, 14488–14496.
- (17) Hu, X.-Y.; Gao, L.; Mosel, S.; Ehlers, M.; Zeller, M.; Jiang, H.; Knauer, S. K.; Wang, L.; Schmuck, C. From Supramolecular Vesicles to Micelles: Controllable Construction of Tumor-Targeting Nanocarriers Based on Host-Guest Interaction between a Pillar[5]-

arene-Based Prodrug and a RGD-Sulfonate Guest. *Small* **2018**, *14*, No. e1803952.

(18) Zhang, Y. M.; Liu, Y. H.; Liu, Y. Cyclodextrin-based multistimuli-responsive supramolecular assemblies and their biological functions. *Adv. Mater.* **2020**, *32*, 1806158.

(19) Zhang, Y.-M.; Xu, Q.-Y.; Liu, Y. Molecular recognition and biological application of modified β -cyclodextrins. *Sci. China. Chem.* **2019**, *62*, 549–560.

(20) Yu, G.; Zhao, X.; Zhou, J.; Mao, Z.; Huang, X.; Wang, Z.; Hua, B.; Liu, Y.; Zhang, F.; He, Z.; Jacobson, O.; Gao, C.; Wang, W.; Yu, C.; Zhu, X.; Huang, F.; Chen, X. Supramolecular Polymer-Based Nanomedicine: High Therapeutic Performance and Negligible Long-Term Immunotoxicity. *J. Am. Chem. Soc.* **2018**, *140*, 8005–8019.

(21) Lovell, J. F.; Liu, T. W. B.; Chen, J.; Zheng, G. Activatable photosensitizers for imaging and therapy. *Chem. Rev.* **2010**, *110*, 2839–2857.

(22) Wilson, B. C.; Patterson, M. S. The physics, biophysics and technology of photodynamic therapy. *Phys. Med. Biol.* **2008**, *53*, R61–R109.

(23) Deng, K.; Li, C.; Huang, S.; Xing, B.; Jin, D.; Zeng, Q.; Hou, Z.; Lin, J. Recent progress in near infrared light triggered photodynamic therapy. *Small* **2017**, *13*, 1702299.

(24) Celli, J. P.; Spring, B. Q.; Rizvi, I.; Evans, C. L.; Samkoe, K. S.; Verma, S.; Pogue, B. W.; Hasan, T. Imaging and photodynamic therapy: mechanisms, monitoring, and optimization. *Chem. Rev.* **2010**, *110*, 2795–2838.

(25) Mavridis, I. M.; Yannakopoulou, K. Porphyrinoid-Cyclodextrin Assemblies in Biomedical Research: An Update. *J. Med. Chem.* **2020**, *63*, 3391–3424.

(26) Li, S.-Y.; Cheng, H.; Xie, B.-R.; Qiu, W.-X.; Zeng, J.-Y.; Li, C.-X.; Wan, S.-S.; Zhang, L.; Liu, W.-L.; Zhang, X.-Z. Cancer Cell Membrane Camouflaged Cascade Bioreactor for Cancer Targeted Starvation and Photodynamic Therapy. *ACS Nano* **2017**, *11*, 7006–7018.

(27) Ji, C.; Gao, Q.; Dong, X.; Yin, W.; Gu, Z.; Gan, Z.; Zhao, Y.; Yin, M. A Size-Reducible Nanodrug with an Aggregation-Enhanced Photodynamic Effect for Deep Chemo-Photodynamic Therapy. *Angew. Chem., Int. Ed.* **2018**, *57*, 11384–11388.

(28) Lee, E.; Li, X.; Oh, J.; Kwon, N.; Kim, G.; Kim, D.; Yoon, J. A boronic acid-functionalized phthalocyanine with an aggregation-enhanced photodynamic effect for combating antibiotic-resistant bacteria. *Chem. Sci.* **2020**, *11*, 5735–5739.

(29) Jin, J.; Zhu, Y.; Zhang, Z.; Zhang, W. Enhancing the Efficacy of Photodynamic Therapy through a Porphyrin/POSS Alternating Copolymer. *Angew. Chem., Int. Ed.* **2018**, *57*, 16354–16358.

(30) He, C.; Liu, D.; Lin, W. Self-assembled core-shell nanoparticles for combined chemotherapy and photodynamic therapy of resistant head and neck cancers. *ACS Nano* **2015**, *9*, 991–1003.

(31) Mao, W.; Liao, Y.; Ma, D. Supramolecular Assembly Mediated by Host-Guest Interaction for Improved Chemo-Photodynamic Combination Therapy. *Chem. Commun.* **2020**, *56*, 4192–4195.

(32) Lim, W. Q.; Yang, G.; Phua, S. Z. F.; Chen, H.; Zhao, Y. Self-Assembled Oxaliplatin (IV) Prodrug-Porphyrin Conjugate for Combinational Photodynamic Therapy and Chemotherapy. *ACS Appl. Mater. Interfaces* **2019**, *11*, 16391–16401.

(33) Phua, S. Z. F.; Xue, C.; Lim, W. Q.; Yang, G.; Chen, H.; Zhang, Y.; Wijaya, C. F.; Luo, Z.; Zhao, Y. Light-Responsive Prodrug-Based Supramolecular Nanosystems for Site-Specific Combination Therapy of Cancer. *Chem. Mater.* **2019**, *31*, 3349–3358.

(34) Chen, H.; Zeng, X.; Tham, H. P.; Phua, S. Z. F.; Cheng, W.; Zeng, W.; Shi, H.; Mei, L.; Zhao, Y. NIR-Light-Activated Combination Therapy with a Precise Ratio of Photosensitizer and Prodrug Using a Host-Guest Strategy. *Angew. Chem., Int. Ed.* **2019**, *131*, 7723–7728.

(35) Li, Z.-Q.; Zhang, Y.-M.; Chen, H.-Z.; Zhao, J.; Liu, Y. Hierarchical organization of spherical assembly with reversibly photocontrollable cross-links. *J. Org. Chem.* **2013**, *78*, 5110–5114.

(36) Sun, H.-L.; Chen, Y.; Zhao, J.; Liu, Y. Photocontrolled Reversible Conversion of Nanotube and Nanoparticle Mediated by β -Cyclodextrin Dimers. *Angew. Chem., Int. Ed.* **2015**, *54*, 9376–9380.

(37) Kano, K.; Nishiyabu, R.; Asada, T.; Kuroda, Y. Static and dynamic behavior of 2: 1 inclusion complexes of cyclodextrins and charged porphyrins in aqueous organic media. *J. Am. Chem. Soc.* **2002**, *124*, 9937–9944.

(38) Liu, G.; Xu, X.; Chen, Y.; Wu, X.; Wu, H.; Liu, Y. A highly efficient supramolecular photoswitch for singlet oxygen generation in water. *Chem. Commun.* **2016**, *52*, 7966–7969.

(39) Liu, Y.; Ke, C.-F.; Zhang, H.-Y.; Cui, J.; Ding, F. Complexation-induced transition of nanorod to network aggregates: alternate porphyrin and cyclodextrin arrays. *J. Am. Chem. Soc.* **2008**, *130*, 600–605.

(40) Zhang, Y.-M.; Yang, Y.; Zhang, Y.-H.; Liu, Y. Polysaccharide nanoparticles for efficient siRNA targeting in cancer cells by supramolecular p K a shift. *Sci. Rep.* **2016**, *6*, 1–11.

(41) Eftink, M. R.; Andy, M. L.; Bystrom, K.; Perlmutter, H. D.; Kristol, D. S. Cyclodextrin inclusion complexes: studies of the variation in the size of alicyclic guests. *J. Am. Chem. Soc.* **1989**, *111*, 6765–6772.

(42) Huang, P.; Wang, D.; Su, Y.; Huang, W.; Zhou, Y.; Cui, D.; Zhu, X.; Yan, D. Combination of small molecule prodrug and nanodrug delivery: amphiphilic drug-drug conjugate for cancer therapy. *J. Am. Chem. Soc.* **2014**, *136*, 11748–11756.

(43) Yang, Y.; Zhang, Y.-M.; Chen, Y.; Chen, J.-T.; Liu, Y. Targeted polysaccharide nanoparticle for adampatin prodrug delivery. *J. Med. Chem.* **2013**, *56*, 9725–9736.

(44) Phua, S. Z. F.; Yang, G.; Lim, W. Q.; Verma, A.; Chen, H.; Thanabalu, T.; Zhao, Y. Catalase-integrated hyaluronic acid as nanocarriers for enhanced photodynamic therapy in solid tumor. *ACS Nano* **2019**, *13*, 4742–4751.

(45) Liu, X.; Shao, W.; Zheng, Y.; Yao, C.; Peng, L.; Zhang, D.; Hu, X. Y.; Wang, L. GSH-Responsive supramolecular nanoparticles constructed by β -D-galactose-modified pillar[5]arene and camptothecin prodrug for targeted anticancer drug delivery. *Chem. Commun.* **2017**, *53*, 8596–8599.

(46) Sun, G.; He, Z.; Hao, M.; Xu, Z.; Hu, X.-Y.; Zhu, J.-J.; Wang, L. Bifunctional supramolecular prodrug vesicles constructed from a camptothecin derivative with a water-soluble pillar[5]arene for cancer diagnosis and therapy. *Chem. Commun.* **2019**, *55*, 10892–10895.

(47) Zhang, Y.; Yang, D.; Chen, H.; Lim, W. Q.; Phua, F. S. Z.; An, G.; Yang, P.; Zhao, Y. Reduction-sensitive fluorescence enhanced polymeric prodrug nanoparticles for combinational photothermal-chemotherapy. *Biomaterials* **2018**, *163*, 14–24.

(48) Fu, H.-G.; Chen, Y.; Yu, Q.; Liu, Y. A tumor-targeting Ru/polysaccharide/protein supramolecular assembly with high photodynamic therapy ability. *Chem. Commun.* **2019**, *55*, 3148–3151.

(49) Yu, G.; Cen, T.-Y.; He, Z.; Wang, S.-P.; Wang, Z.; Ying, X.-W.; Li, S.; Jacobson, O.; Wang, S.; Wang, L.; Lin, L.-S.; Tian, R.; Zhou, Z.; Ni, Q.; Li, X.; Chen, X. Porphyrin Nanocage-Embedded Single-Molecular Nanoparticles for Cancer Nanotheranostics. *Angew. Chem., Int. Ed.* **2019**, *58*, 8799–8803.

(50) Chou, T.-C. Drug Combination Studies and Their Synergy Quantification Using the Chou-Talalay Method. *Cancer Res.* **2010**, *70*, 440–446.